Multispectral coherence: Which decomposition should we use?

Bin Lyu[1], Jie Qi[1], Fangyu Li[2], Ying Hu[3], Tao Zhao[1], Sumit Verma[4], and Kurt J. Marfurt[1]

Abstract

Seismic coherence is commonly used to delineate structural and stratigraphic discontinuities. We generally use full-bandwidth seismic data to calculate coherence. However, some seismic stratigraphic features may be buried in this full-bandwidth data but can be highlighted by certain spectral components. Due to thin-bed tuning phenomena, discontinuities in a thicker stratigraphic feature may be tuned and thus better delineated at a lower frequency, whereas discontinuities in the thinner units may be tuned and thus better delineated at a higher frequency. Additionally, whether due to the seismic data quality or underlying geology, certain spectral components exhibit higher quality over other components, resulting in correspondingly higher quality coherence images. Multispectral coherence provides an effective tool to exploit these observations. We have developed the performance of multispectral coherence using different spectral decomposition methods: the continuous wavelet transform (CWT), maximum entropy, amplitude volume technique (AVT), and spectral probe. Applications to a 3D seismic data volume indicate that multispectral coherence images are superior to full-bandwidth coherence, providing better delineation of incised channels with less noise. From the CWT experiments, we find that providing exponentially spaced CWT components provides better coherence images than equally spaced components for the same computation cost. The multispectral coherence image computed using maximum entropy spectral voices further improves the resolution of the thinner channels and small-scale features. The coherence from AVT data set provides continuous images of thicker channel boundaries but poor images of the small-scale features inside the thicker channels. Additionally, multispectral coherence computed using the nonlinear spectral probes exhibits more balanced and reveals clear small-scale geologic features inside the thicker channel. However, because amplitudes are not preserved in the nonlinear spectral probe decomposition, noise in the noisier shorter period components has an equal weight when building the covariance matrix, resulting in increased noise in the generated multispectral coherence images.

Introduction

Seismic coherence is a measure of the similarity between the waveforms or traces in seismic data volumes. It is a powerful tool to delineate seismic discontinuities such as faults and stratigraphic edges, incoherent zones such as the karst collapse and mass transport complexes, as well as areas contaminated by seismic noise. Bahorich and Farmer (1995) evaluate 3D seismic discontinuity coherence by calculating the maximum crosscorrelation value with neighboring traces. Marfurt et al. (1998) develop a more robust coherence estimation method, which is based on a multitrace semblance algorithm, to improve the noise reduction ability. Gerszten-korn and Marfurt (1999) introduce another coherence calculation method, which is realized by calculating the energy ratio between the dominant eigenvalues and the sum of all eigenvalues of the covariance matrix, to improve the lateral resolution. Marfurt et al. (1999) further improve the algorithm, which considers the structural dip effect on the coherence estimation, to provide better results.

Coherence is generally calculated from the full-bandwidth seismic data. The quality of the coherence images is dependent on the quality of the input seismic data, which could be improved using structure-oriented filtering (SOF), spectral balancing, and other postmigration data conditioning methods (Chopra and Marfurt, 2007). Furthermore, different spectral components often illuminate different geologic features (Partyka et al., 1999), where Peyton et al. (1998) find that the 36 Hz spectral

component image among the results between 20 and 50 Hz could best delineate the edges of incised valleys in a Red Fork, Oklahoma Formation. Marfurt and Kirlin (2001) and Laughlin et al. (2002) show that the thickness of the channels is strongly related with their spectral amplitude due to the thickness tuning: A lower peak frequency indicates thicker formations, whereas a higher peak frequency indicates thinner formations. Zeng (2015) interprets the spatial geometry and stacking pattern of seismically thin beds using a seismic sedimentology-based approach. An observation was obtained from a synthetic model that one can characterize a thin-bed depositional system by a seismic-geomorphologic pattern of the same spatial shape on sequential relative geologic time slices, but the amplitude, phase, and polarity would vary depending on the estimated seismic wavelet. Hardage (2009) and Lyu et al. (2018) report that certain spectral components of the seismic data provide higher quality results over the other components.

Alaei (2012) and Li and Lu (2014) compute coherence from different spectral components and corendered them using red, green, and blue (RGB) blending to illuminate channels, caves, and karsts. Wang et al. (2018) develop a 3D geosteering coherence attribute and use it to detect deep-formation discontinuities. Wang et al. (2019) further use the multispectral-phase information to combine the geosteering coherence and display the result using RGB blending. Noticing that such analysis was limited to only three spectral coherence volumes, Marfurt (2017) and Li et al. (2018) generalize these concepts by introducing what they called multispectral coherence, in which the covariance matrices from each band-pass-filtering bank are added prior to computing the coherence attribute. The case studies of channel boundary highlighting (Li et al., 2018) and fault enhancement (Lyu et al., 2019) indicate the effectiveness of this multispectral coherence method. Qi et al. (2019) and Chopra and Marfurt (2019) generalize this concept further to compute coherence not only from multiple spectral components but also from multiple azimuth and offset components.

There are several popular seismic spectral decomposition algorithms including the continuous wavelet transform (CWT) (Sinha et al., 2005), matching pursuit (Castagna et al., 2003; Liu and Marfurt, 2007), and a technique based on maximum entropy called constrained least-squares spectral analysis (Puryear et al., 2012). This latter approach has superior time and frequency resolution. Other techniques are similar to spectral decomposition in that they enhance certain window spectral components to facilitate the identification of lateral discontinuities and vertical unconformities but do not attempt to reconstruct the original data. Gao (2013) introduces a spectral probe technique, which crosscorrelates sines and cosines with the seismic data and outputs the crosscorrelation coefficient as an attribute. A related (also nonlinear) technique is called the amplitude volume technique (AVT) (Bulhões, 1999; Bulhões and de Amorin, 2005), which enhances low-frequency information in the seismic data.

Although more expensive than computing coherence from a single full-bandwidth seismic volume, multispectral coherence provides significantly enhanced images. In this paper, we first examine which multispectral coherence provides better images: computed using equally or exponentially sampled frequencies. We further examine whether multispectral coherence computed from the high-resolution maximum entropy spectral decomposition provides higher resolution images. Besides the CWT and maximum entropy decomposition methods, we augment this relatively long list of decomposition algorithms with the nonlinear spectral probe and AVT methods.

We begin our paper by illustrating the generalized workflow used to compute the multispectral coherence from the original full-bandwidth seismic data. We then discuss the theory of seismic spectral decomposition methods. Next, we evaluate these methods using a 3D seismic data volume with a complex suite of incised channels, acquired over the southwest coast of North Island, New Zealand. Finally, we conclude with a summary of our comments and recommendations.

Method
Multispectral coherence workflow

In Figure 1, we show the workflow to compute the multispectral coherence attribute on the decomposed spectral components from the original full-bandwidth seismic data. The quality of the coherence images is dependent on the quality of the input seismic data. Chopra and Marfurt (2007) give suggestions to improve the seismic data quality using some postmigration data-conditioning methods.

There are different types of noise in the coherence images. Marfurt and Alves (2014) discuss the pitfalls in seismic interpretation caused by seismic noise and processing errors. The coherence images may suffer from two categories of noise: seismic noise and "geology" noise.

Seismic noise, for example, the acquisition footprint, random noise, and migration aliasing, plays a negative role in delineating geologic features. The quality of the coherence images is definitely decreased in the presence of such noise, which is expected to be suppressed before coherence computation.

Another type of noise in coherence images is from chaotic geology features such as fault damage zones, or condensed sections, etc. These features also exhibit discontinuities in the coherence images, which should always be preserved. They are considered as geology "noise" if we try to delineate the incised channel boundaries, but they may be geologic indicators for other geology purposes (Marfurt and Alves, 2014).

In our workflow, we first perform SOF on the input full-bandwidth seismic amplitude volume, to suppress the seismic noise and improve the data quality. SOF

is a robust filtering method, avoiding the smearing of faults, fractures, and other seismic discontinuities.

Next, we decompose the full-bandwidth seismic data after SOF into different spectral components. We evaluate several different spectral decomposition methods, including not only CWT and maximum entropy decomposition but also the AVT and spectral probe methods.

We then build the covariance matrix, to combine multiple coherence attributes together into a single volume. Dewett and Henza (2015) use a self-organizing map method for combination. Sui et al. (2015) compute coherence using only the spectral magnitudes without phase information, which could not handle complicated structures. To improve adaptability, we follow Marfurt (2017) in building the covariance matrix using the spectral voices, considering the spectral magnitude and phase information.

The spectral voices are defined as

$$u(f_l, t_k, x_m, y_m) = a(f_l, t_k, x_m, y_m) \exp[i\varphi(f_l, t_k, x_m, y_m)], \quad (1)$$

where u represents the spectral voice of frequency f, a is the magnitude component, φ denotes the phase component, and l is the component number. The term t_k denotes the structurally interpolated time sample at a distance (x_m, y_m) from the coordinate origin point.

The spectral voice u in equation 1 and the corresponding analytic trace u^H are used to compute each element C_{mn} of the covariance matrix **C** along the structures, which considers the magnitude and phase components:

$$C_{mn} = \sum_{l=1}^{L} \sum_{k=-K}^{K} [u(t_k, f_l, x_m, y_m)u(t_k, f_l, x_n, y_n) \\ + u^H(t_k, f_l, x_m, y_m)u^H(t_k, f_l, x_n, y_n)]. \quad (2)$$

We use equation 2 to build the covariance matrix from different spectral components, which adapts to complicated geologic structures. For a specific spectral component, we can improve the quality of particular structures in the coherence image because the signal appears stronger than noise, further resulting in an improvement in the combined coherence attribute.

The final step is to compute the coherence attributes on the generated covariance matrix. The fact that coherence should be computed along structural dip has been known for some time (Marfurt et al., 1999). In our research, we used a gradient structure tensor method to compute the inline and crossline dip attributes for the following coherence computation. We can output the
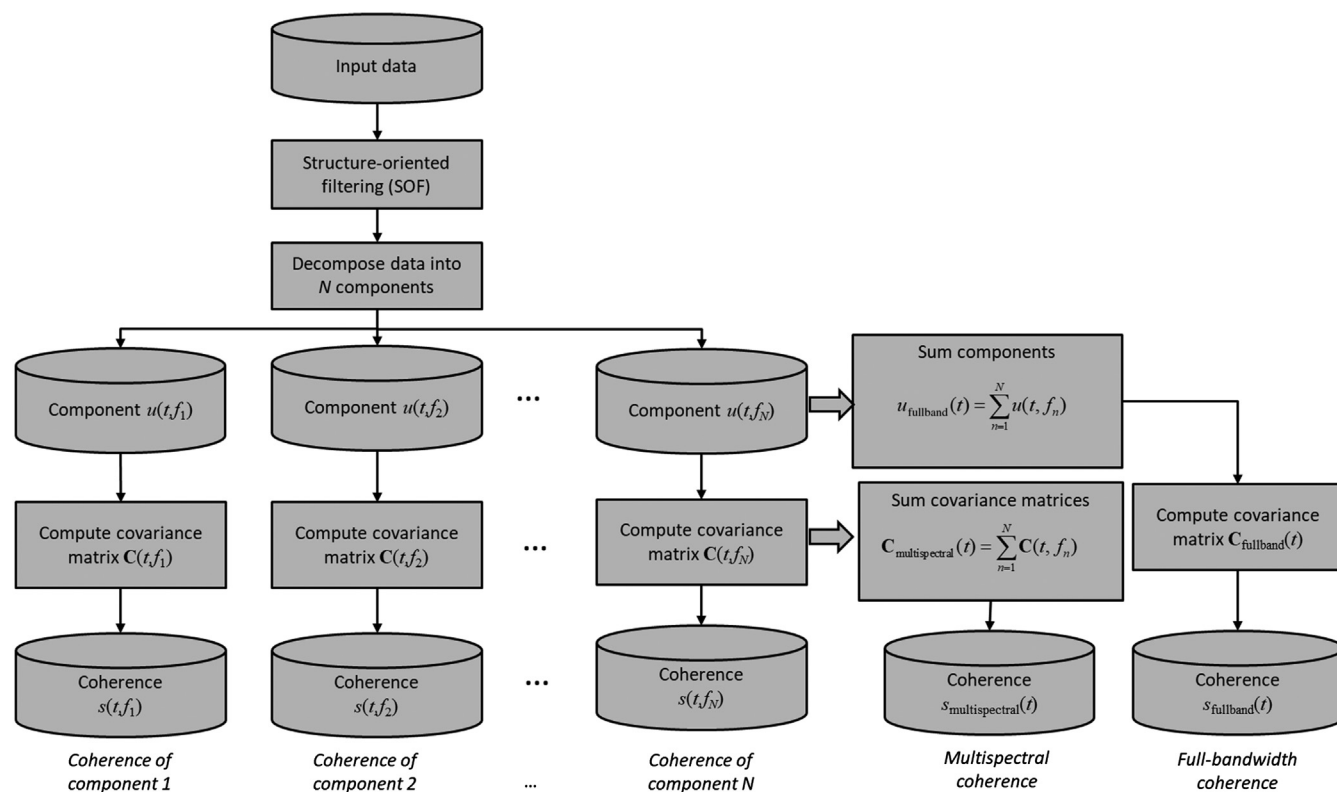

Figure 1. A workflow showing the computation of multispectral coherence from the original full-bandwidth seismic data. In this paper, we evaluate the impact of alternative decomposition algorithms, including CWT of equal-spacing and exponential-spacing, and maximum entropy spectral decomposition that can reconstruct the original seismic data. We also evaluate the impact of several nonlinear decomposition algorithms, including the AVT and spectral probe, which cannot reconstruct the original data (the figure is modified from Marfurt, 2017).

coherence volumes from each spectral component and the combined multispectral coherence data set. In our research, we use the energy-ratio method of Gerszten-korn and Marfurt (1999) for coherence computation,

Figure 2. The location of the Tui3D seismic survey (the orange star) and the structural style of the offshore Taranaki Basin, New Zealand (after King et al., 1993; Infante-Paez and Marfurt, 2017; Lubo-Robles and Marfurt, 2019). The data are acquired by Veritas DGC Australia Pty in 2003, covering approximately 352 km². The acquisition parameters are streamer separation 150 m, source separation 75 m, bin size 12.5×12.5 m, and time sample rate 4 ms.

Figure 3. (a) A representative vertical slice AA′ and (b) time slice at $t = 2.16$ s through the seismic amplitude volume at the level of several incised channels (the green arrows in b).

which is also used to provide the input for the fault skeletonization (Qi et al., 2016, 2019). This coherence computation method is realized by calculating the energy ratio between the dominant eigenvalues and the sum of all eigenvalues of the covariance matrix. The details of the energy-ratio method are shown in Appendix A.
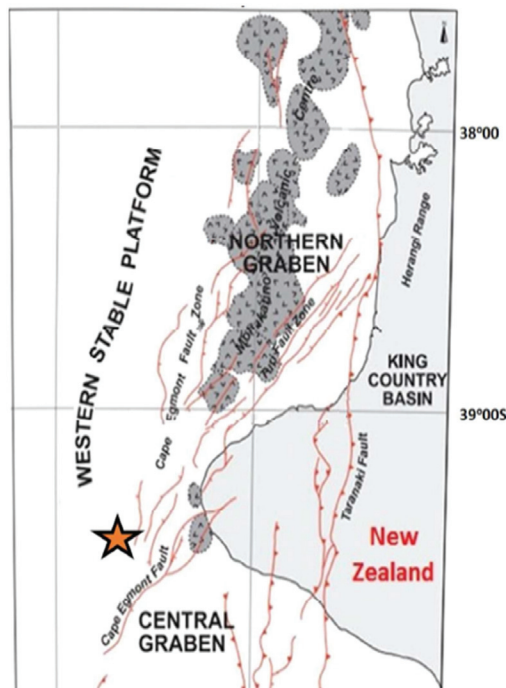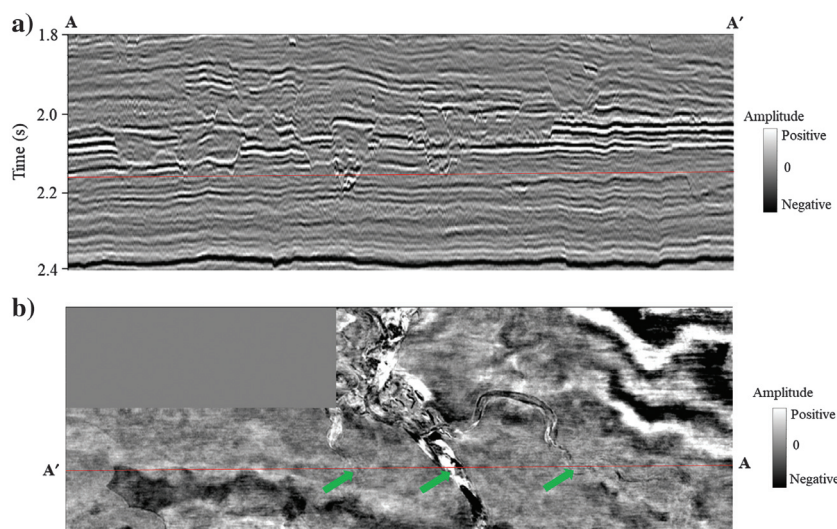
Seismic spectral decomposition algorithms

Seismic spectral decomposition (Partyka et al., 1999) is an important step in the multispectral coherence computation workflow (Figure 1). We can decompose the full-bandwidth seismic data into different spectral components using linear or nonlinear decomposition methods. In our research, we first evaluate the application of CWT and maximum entropy decomposition methods for multispectral coherence computation, which could reconstruct the original full-bandwidth seismic data.

CWT is defined based on the scaled and shifted versions of a "mother wavelet," which is a complex exponential of a frequency within a Gaussian temporal window (Grossmann and Morlet, 1984). We perform CWT by first crosscorrelating the library of these wavelets with seismic traces followed by summation over time (Appendix B). CWT is widely used in seismic interpretation, for example, Matos and Marfurt (2011) indicate that we can use the Morlet complex wavelet transform to detect the phase discontinuities and Davogustto et al. (2013) use the spectral ridges and phase residues to correlate with subtle stratigraphic features.

CWT provides time-scale maps instead of the time-frequency spectrum produced by the short-time Fourier transform over a chosen time window. Mother wavelet selection is critical for CWT decomposition. Some factors should be considered during the selection procedure, such as the vertical resolution reduction due to the side lobes of the wavelet (Castagna and Sun, 2006), even though there is not an optimum wavelet among the commonly used ones. The short-time Fourier transform uses a window with predefined length to produce a time-frequency spectrum, which has a fixed time-frequency resolution. On the contrary, there is no requirement of predefining the window length in the CWT method, resulting in a better time resolution at higher frequencies and a better frequency resolution at lower frequencies.

However, the application of a sliding temporal window in CWT limits the temporal and frequency resolutions. Puryear et al. (2012) analyze this fundamental issue in spectral decomposition using a thin-layer model surrounded by strong reflections. They observe that a short window is required to avoid the interference, but a long enough window is preferable to avoid incorrect estimation of

the notch location due to the window-smearing effect on the spectrum. If we try to improve the frequency resolution, a longer window length is desirable but results in poor time resolution.

To further improve the time and frequency resolution of the CWT spectral analysis, we use a maximum entropy implementation of the short-time Fourier transform to decompose full-bandwidth seismic data and compute multispectral coherence. To reduce this window effect in seismic spectral analysis, the maximum entropy algorithm solves an inverse problem using an objective function to fit the data with the minimum of sines and cosines. Different empirical criteria can be used in inversion-based spectral analysis, for example, Portniaguine and Castagna (2004) use an iteratively reweighted least-squares regularization algorithm to invert the normal equations for approaching the seismic wavelet decomposition problem. We follow the constrained least-squares spectral analysis method of Puryear et al. (2012), to compute the Fourier series coefficients as a function of time, which is inverted based on a basis of truncated sinusoidal kernels for a moving time window. It reduces the window smearing and provides a better resolution over the short-time Fourier transform and CWT. An important parameter in this iterative spectral analysis method is the number of iterations. A larger number of iterations provide more accurate least-squares approximations but consumes more computation time.

Besides the CWT and maximum entropy decomposition methods, we further evaluate two nonlinear spectral decomposition methods: AVT and the spectral probe. Ten Kroode et al. (2013) indicate the benefits of the super-low-frequency information of seismic data. First, it could reduce the side lobes of the wavelet to improve the resolution. Second, it suffers less from attenuation and scattering, which helps the waves to penetrate deeper in the earth. Furthermore, it could assist in background model building for seismic inversion and migration velocity analysis. Additionally, the low-frequency seismic data could help identify some geologic features, such as faults (Hardage, 2009). Bulhões (1999) and Bulhões and de Amorin (2005) develop an AVT method to extract super-low-frequency information from original seismic data. Vernengo and Trinchero (2015) and Vernengo et al. (2017) show several case studies to indicate that the AVT data volume could help highlight geologic features. AVT is realized by a nonlinear conversion of the full-bandwidth seismic data. The steps of the conventional AVT workflow (Bulhões, 1999) include calculation of the root-mean square (rms) of the seismic amplitude

followed by the inverse Hilbert transform. In our research, we develop an optimized workflow using the envelope instead of the seismic amplitude. The details are illustrated in Appendix C.

We further evaluate another nonlinear spectral probe algorithm to decompose full-bandwidth seismic data and produce multispectral coherence images. Gao (2013) originally computes a new attribute using a spectral probe process to improve the precision and resolution of conventional seismic amplitude profiles for geometric interpretation. It is implemented by considering a full wavelength of a cosine wave as a wavelet probe and then crosscorrelating with the seismic data (Appendix D). The spectral probe result can be considered as an approximation of a spectral voice subjected to a short-window automatic gain control in a mathematically loose sense. The outputs of the crosscorrelation are normalized coefficients, ranging from -1.0 to $+1.0$. The generated components using the spectral probe method are insensitive to amplitude variation, and they are acceptable for geometric attribute computation. The wavelet spectral probe analysis has a higher computational efficiency compared with other Fourier transform-based decomposition methods.

Data description

We perform a case study on a 3D field seismic data to evaluate the multispectral coherence computation workflow (Figure 1) using different spectral decomposition methods. The Tui3D seismic survey is located in the southwest coast of the North Island, New Zealand
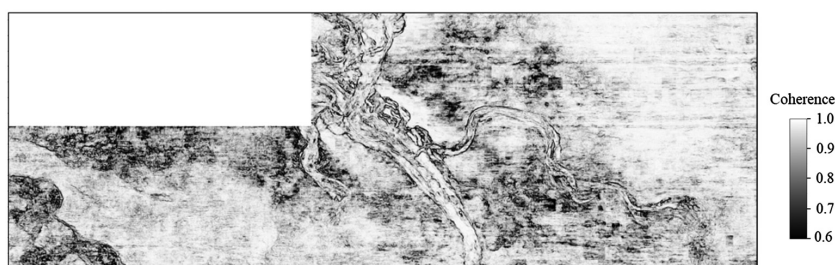

Figure 4. Coherence attribute time slice at 2.16 s computed using the original full-bandwidth seismic data, showing strong noise, which decreases its detectability of the incised channels.
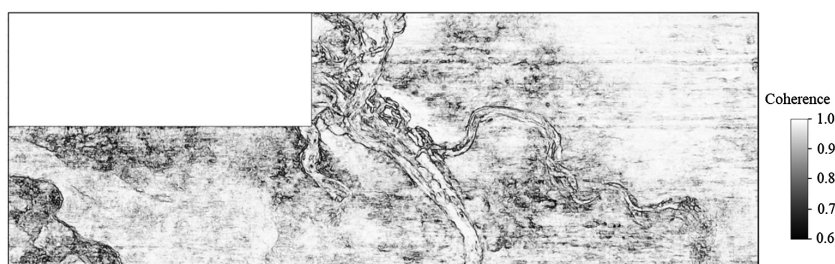

Figure 5. Coherence image computed using the SOF processed full-bandwidth seismic data, showing better quality with less noise compared to the coherence image computed using the original data (Figure 4).

(Figure 2, after King et al., 1993; Infante-Paez and Marfurt, 2017; Lubo-Robles and Marfurt, 2019). The data are acquired by Veritas DGC Australia Pty in 2003, which covers approximately 352 km^2 offshore of the Taranaki Basin. The streamer separation is 150 m, the source separation is 75 m, and the bin size is 12.5 × 12.5 m. The time sample rate of the original seismic data is 4 ms.

The Taranaki Basin is located above the subduction zone where the Pacific Plate is subducting beneath the Australian Plate (Yagci, 2016). The basin contains two primary structural elements: the Eastern Taranaki Graben Complex and the Western Platform. The Tui3D survey is located on the Western Platform, which was affected by the normal block faulting during the Late Cretaceous-Eocene, but it remained relatively stable during most of the Tertiary (Pilaar and Wakefield, 1984; Lubo-Robles and Marfurt, 2019).

The Moki A sands unit is the target in our research, which is deposited as a base of the slope turbidite and is characterized by a major submarine meandering channel complex (Bussell, 1994). A geophysical challenge is how to clearly delineate the boundaries of the incised

Figure 6. (a) The normalized spectrum of the SOF processed data in target area from 1.8 to 2.4 s, (b) the wavelets used in equally spaced CWT with a constant linear increment, including central frequencies 10, 25, 40, 55, 70, and 85 Hz, and (c) the wavelets used in exponentially spaced CWT with a constant octave bandwidth. Note that the lateral axis in (c) indicates the constant exponent increment, resulting in CWT spectral voices with central frequencies of 10, 15, 24, 36, 55, and 85 Hz.

sinusoidal channels, such as the ones shown in a representative vertical slice AA′ (Figure 3a) and time slice at 2.16 s (Figure 3b) indicated by the green arrows in Figure 3b.

Data conditioning

Libak et al. (2017) observe that the coherence attribute has the potential to identify small-scale displacement in the case of noise-free synthetic data, but the detectability will be decreased in the field seismic data due to the presence of noise. This motivates us to perform a noise attenuation process prior to coherence computation to improve the quality of coherence images.

There are several different types of noise attenuation methods. We need to preserve subtle geologic features such as minor channels, which are indicated by small-scale edges in seismic data. We apply SOF on poststack full-bandwidth seismic data, following the suggestion of Chopra and Marfurt (2007). SOF is robust to suppress the incoherent noise and coherent footprint artifacts, but it preserves subtle geologic features.

The original full-bandwidth seismic data (Figure 3a and 3b) are of good quality with a relatively high signal-to-noise ratio, but they still have some random noise, which results in artifacts in the coherence attribute (Figure 4), decreasing its detectability of the incised channels. We performed SOF on the original data to suppress noise. The coherence image computed using SOF-processed data (Figure 5) exhibits better quality with less noise over the result from the original seismic data (Figure 4).

Which spectral voices to choose in multispectral coherence? CWT experiments

We first use the CWT method to decompose full-bandwidth seismic data after SOF into different spectral voices, followed by computation of the energy-ratio coherence for each component. An important issue in multispectral coherence is how to choose the appropriate components for computation among tens of decomposed spectral voices. In Figure 6a, we show the normalized spectrum of the SOF processed data in our target area from 1.8 to 2.4 s. It is noted that the effective frequency bandwidth ranges from approximately 8 to 95 Hz. We choose six CWT spectral voices within the effective bandwidth, starting from the central frequency 10 Hz and ending with 85 Hz. We can use different spacing method for choosing the spectral voices between the starting and ending frequencies. A natural option is to choose equally spaced CWT spectral voices with a constant linear bandwidth. In Figure 6b, we show the series of wavelets used in the equal-spacing method with a constant 15 Hz increment, including central frequencies 10, 25, 40, 55, 70, and 85 Hz. Another alternative to choose the CWT spectral voices is to use the exponentially spaced components with a constant octave bandwidth. We show the wavelets used in the exponential spacing method in Figure 6c, using the same starting and ending frequencies with the equal-spacing
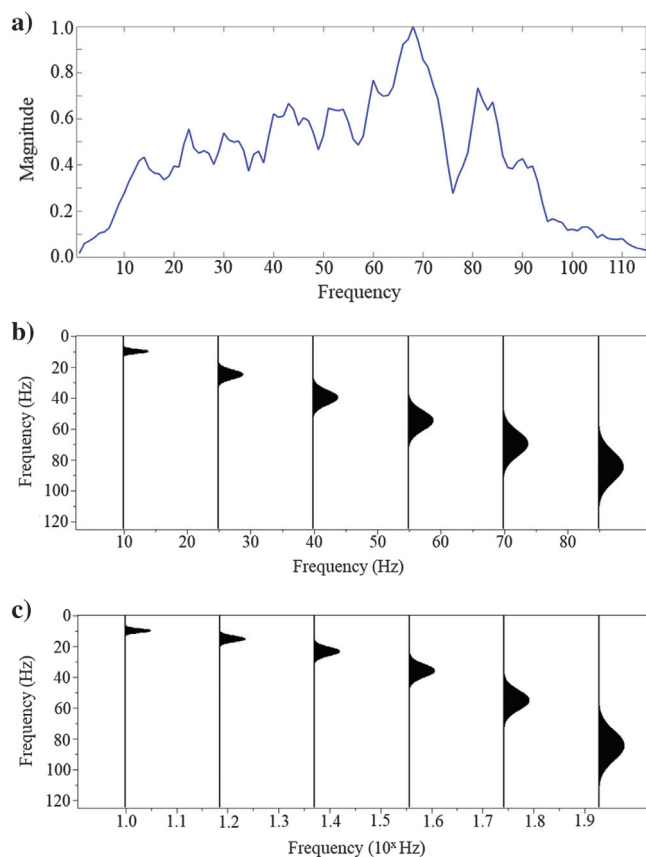
case. The lateral axis in Figure 6c indicates the constant exponent increment in the exponential-spacing method, resulting in spectral voices with the central frequencies 10, 15, 24, 36, 55, and 85 Hz.

In Figure 7, we show coherence images computed using equally spaced CWT spectral voices. It is noted that the channels with different scales are highlighted in the coherence images from different components. The boundaries of the thicker channels are much clearer in the coherence images using the lower frequency voices, such as the 10 (Figure 7a) and 25 Hz (Figure 7b) components, whereas the thinner channels and the geologic details inside the thicker channels are much clearer using the higher frequency voices, such as the coherence images from the 40 (Figure 7c) and 55 Hz (Figure 7d) components. Artifacts associated with the acquisition footprint (the red arrows in Figure 7a, 7e, and 7f) are stronger in the coherence images computed from several spectral voices. The quality seen in Figure 7f for the 85 Hz component is significantly lower, resulting in a coherence image containing less useful information.

We then combine these different coherence volumes into a single coherence data set using the workflow in Figure 1, which is shown in Figure 8. It is noted that this multispectral coherence com-

puted using the equally spaced spectral voices (Figure 8) has less noise (red circles) and clearer channel boundaries (green arrows) over the coherence image computed using the full-bandwidth seismic data (Figure 5). Additionally, the multispectral coherence image reveals more abundant structural details, such as the geologic features inside the thicker channels.

We further use six exponentially spaced CWT spectral voices to compute coherence volumes, which are centered at 10 (Figure 9a), 15 (Figure 9b), 24 (Figure 9c), 36 (Figure 9d), 55 (Figure 9e), and 85 Hz (Figure 9f). The observations from Figure 9 are similar to the coherence images computed using the equally spaced spectral voices (Figure 7). The thicker channels are more high-

Figure 8. Multispectral coherence computed using six equally spaced CWT spectral voices (Figure 7), providing an image with less noise (especially the red circles) and clearer channel boundaries (especially the green arrows) than full-bandwidth coherence (Figure 5).
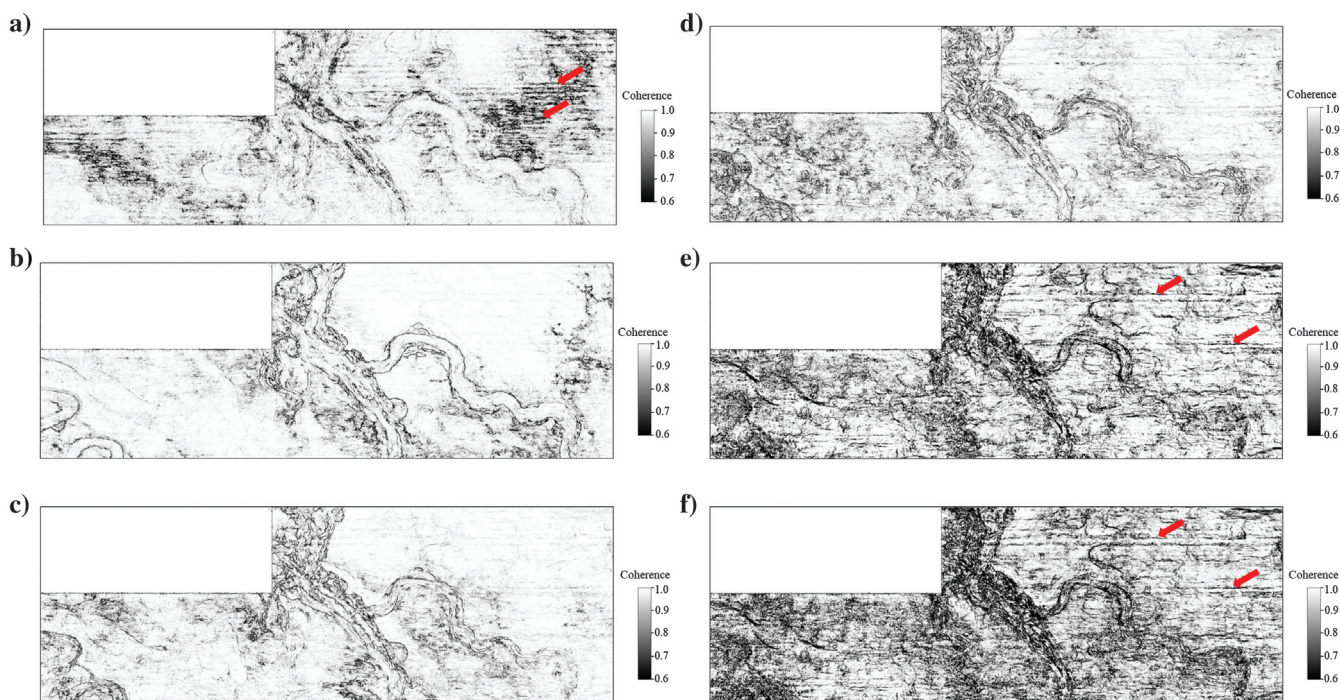

Figure 7. Coherence images computed using six equally spaced CWT spectral voices centered at (a) 10 Hz, (b) 25 Hz, (c) 40 Hz, (d) 55 Hz, (e) 70 Hz, and (f) 85 Hz. Note that the boundaries of the thicker channels are much clearer in coherence images using lower frequency spectral voices, whereas the thinner channels and the geologic details inside the thicker channels are more highlighted using the higher frequency components. Artifacts associated with the acquisition footprint (the red arrows in a, e, and f) are stronger in the coherence images computed from several components. The quality seen in (f) for the 85 Hz component is significantly lower resulting in a coherence image containing less useful information than the other components.

lighted in the coherence images using the lower frequency CWT spectral voices, whereas the higher frequency components provide much clearer images of the thinner channels and small-scale geologic features.

In Figure 10, we show the multispectral coherence image combined using the coherence volumes computed from the exponentially spaced CWT spectral voices using the workflow in Figure 1. We can observe that it appears to be of higher quality over the full-bandwidth result (Figure 5). Especially, it is noted that the multispectral coherence image using exponentially spaced CWT components (Figure 10) exhibits fewer artifacts and clearer channel boundaries (the green arrows in Figure 10) over the multispectral coherence image using equally spaced CWT components (Figure 8). We recommend computing multispectral coherence using exponentially spaced spectral voices.

Coherence on maximum entropy decomposed components

We further use the maximum entropy method to improve the resolution of the CWT spectral voices by reducing the window smearing effect in the spectral analysis (Puryear et al., 2012). We choose the exponentially spaced maximum entropy spectral voices to compute multispectral coherence.

The coherence images computed from each maximum entropy spectral voice are shown in Figure 11, using the same starting and ending frequencies with the ones in the CWT experiments. We take the 15 Hz spectral voice component for example to compare the coherence images computed using the maximum entropy (Figure 11b) and CWT (Figure 9b) spectral voices. It is noted that the coherence from the maximum entropy spectral voice (Figure 11b) provides much more detail and exhibits higher resolution (the red circle) of the channel boundaries over the coherence using the corresponding CWT component (Figure 9b). We can get similar observations from the comparison of other lower frequency spectral voice components. We then
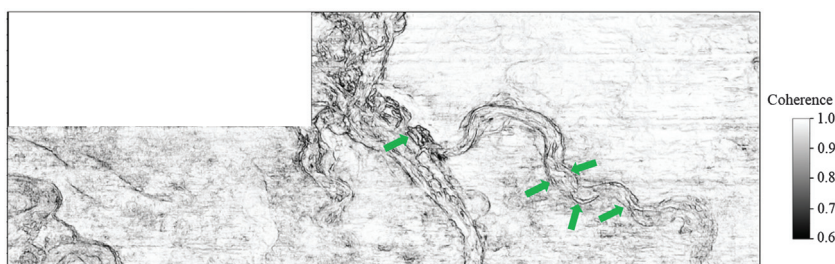

Figure 10. Multispectral coherence computed using six exponentially spaced CWT components (Figure 9). Note that it exhibits fewer artifacts and clearer channel boundaries (the green arrows) over multispectral coherence using equally spaced CWT components (Figure 8).
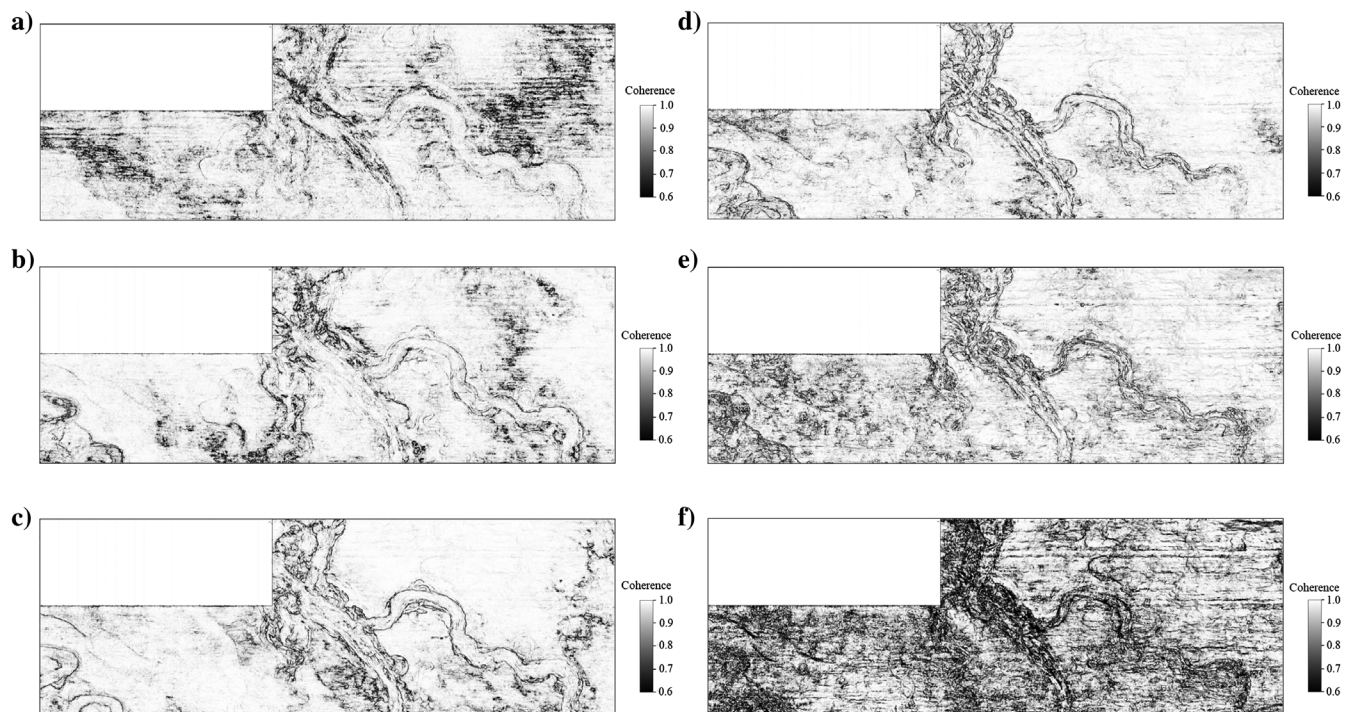

Figure 9. Coherence images computed using exponentially spaced CWT components with central frequencies at (a) 10 Hz, (b) 15 Hz, (c) 24 Hz, (d) 36 Hz, (e) 55 Hz, and (f) 85 Hz. The observations are similar with Figure 7, indicating that thicker channels are more highlighted in lower frequency CWT spectral voices, whereas the higher frequency components provide much clearer images of the thinner channels and small-scale geologic features. Noise in the 85 Hz component coherence (Figure 9f) is much stronger than other components.

generate multispectral coherence (Figure 12) using the maximum entropy spectral voices, which exhibits higher resolution of small-scale features (the green arrows in Figure 12) over the multispectral coherence image computed from the corresponding CWT components (Figure 10).

In Figure 13, we use an example of the enlarged vertical amplitude slice to illustrate the reason why the multispectral coherence works. Figure 13b and 13c shows the 24 and 36 Hz spectral voice components using the maximum entropy decomposition from the full-bandwidth seismic amplitude (Figure 13a). Compared with the full-bandwidth data (the red circles in Figure 13a), the boundaries of the thicker channels are much sharper in the 24 Hz component (the red circles in Figure 13b), whereas the thinner channel boundaries are sharper and clearer in the 36 Hz spectral voice (the red circles in Figure 13c). The channels with different scales are more highlighted in specific spectral voices, resulting in improved images of channel boundaries in the multispectral coherence.

Coherence on AVT data volume

We use an optimized nonlinear AVT algorithm (Appendix C) to extract the super-low-frequency information (window length 16 ms), which helps delineate

large-scale geologic features. AVT produces only one data volume, not several different spectral components, which requires a relatively low computation cost and small storage of the following energy-ratio coherence calculation over other spectral decomposition methods.

The AVT time slice is shown in Figure 14a, which contains less noise and weaker reflections compared to the original seismic amplitude time slice (Figure 3b). We then use this AVT data set to compute the energy-ratio coherence attribute, which is shown in Figure 14b. It is clearer with less noise than coherence computed using the SOF full-bandwidth seismic data (Figure 5).It especially provides more continuous boundaries of the thicker channels (the green arrows in Figure 14b) compared with the coherence images computed from other
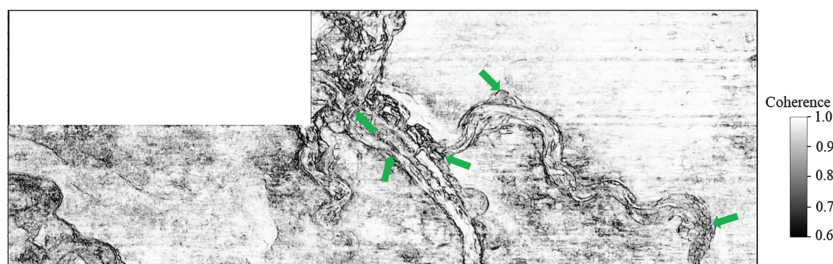

Figure 12. Multispectral coherence image computed using maximum entropy spectral voice components, exhibiting higher resolution of small-scale features (the green arrows) compared with the multispectral coherence image computed from the corresponding CWT components (Figure 10).
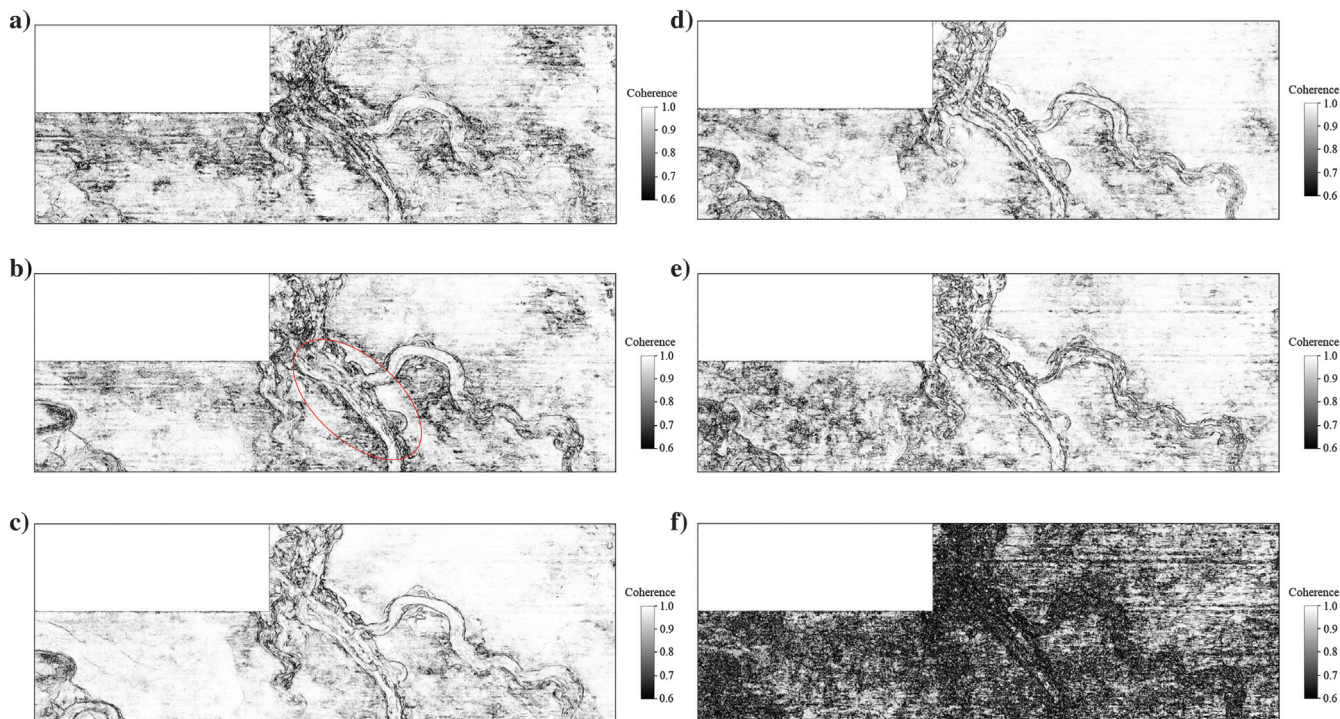

Figure 11. Coherence images computed using maximum entropy spectral voice components at (a) 10 Hz, (b) 15 Hz, (c) 24 Hz, (d) 36 Hz, (e) 55 Hz, and (f) 85 Hz. Note that the coherence images from the lower frequency maximum entropy spectral voices provide more details and exhibit higher resolution of the channel boundaries than coherence images using the corresponding CWT components, such as the red circle area in (b) compared with Figure 9b.

spectral decomposition methods. However, imaging of small-scale features inside thicker channels is decreased due to the lack of higher frequency components in AVT data.

Coherence on spectral probes

The wavelet spectral probe analysis produces spectral voice components from the full-bandwidth seismic data with high computational efficiency. In Figure 15, we show an example of the decomposed spectral voice using the period 36 Hz. It is noted that the spectral

probe is insensitive to the amplitude variation. In a mathematically loose sense, the result approximates a spectral voice that has been subjected to a short-window automatic gain control. The energy is much more balanced than other spectral decomposition methods. The spectral probe components are available for seismic geometric attribute calculation, such as coherence.

We decompose the full-bandwidth seismic data into six spectral probes using period 10, 15, 24, 36, 55, and 85 Hz. We then use these spectral probes to compute the multispectral coherence (Figure 16). Besides

Figure 13. (a) Enlarged full-bandwidth vertical seismic amplitude slice. (b) 24 Hz spectral voice and (c) 36 Hz spectral voice after maximum entropy decomposition. Compared with full-bandwidth data (the red circles in a), the boundaries of the thicker channels are much sharper in the 24 Hz component (the red circles in b), whereas the thinner channel boundaries are sharper and clearer in the 36 Hz spectral voice (the red circles in c). The channels with different scales are more highlighted in specific spectral voices, resulting in the improved images of channel boundaries in multispectral coherence.
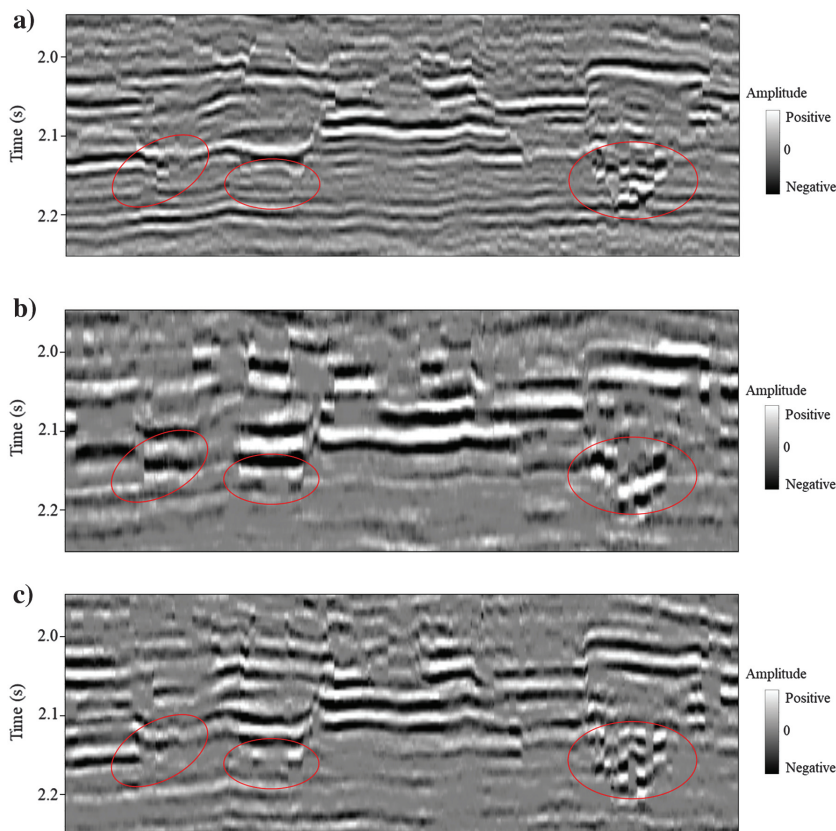

Figure 14. (a) AVT time slice, showing less noise and weaker reflections compared with the original seismic amplitude time slice (Figure 3b). (b) Coherence attribute computed using the AVT volume, behaving much clearer with less noise over coherence computed using the SOF full-bandwidth seismic data (Figure 5). Note the more continuous boundaries of the thicker channels (the green arrows in b) compared with the coherence images computed from other spectral decomposition methods. However, the imaging of some small-scale features inside the thicker channels is decreased due to the lack of higher frequency components in the AVT data.
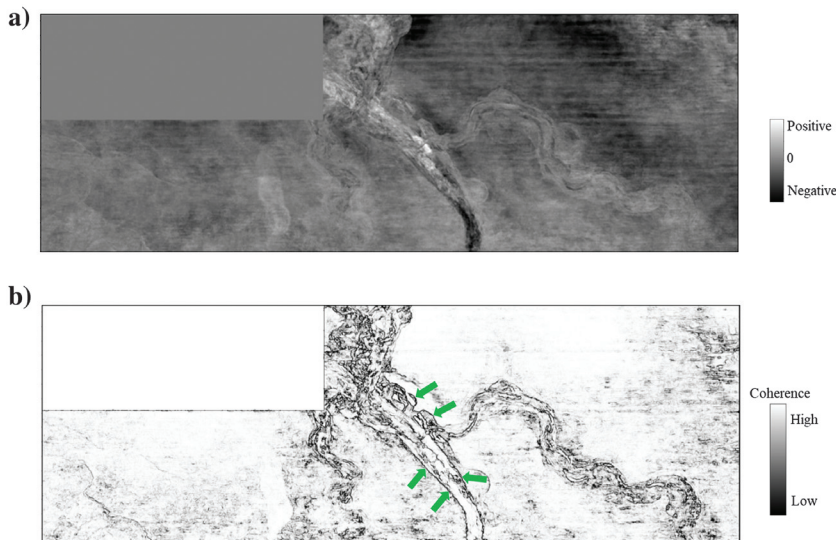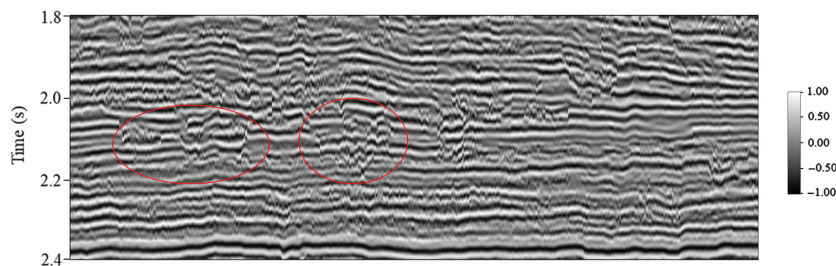
Figure 15. Vertical slice of the spectral probe component using period 36 Hz, which is insensitive to the amplitude variation, and the energy is much more balanced than other spectral decomposition methods, especially the channels indicated by the red circles.

Figure 16. Multispectral coherence image computed using six spectral probes. It exhibits more balanced than the multispectral coherence images from other spectral decomposition methods but is noisier due to the equal weight for the noise in the shorter period components when we build the covariance matrix (the red circles).

improvement over the full-bandwidth coherence image (Figure 5), multispectral coherence images computed using spectral probes (Figure 16) are more balanced than multispectral coherence images from other spectral decomposition methods. However, because amplitudes are not preserved in spectral probes, we use an equal weight for the noise in the noisier shorter period components when we build the covariance matrix. This increases the noise in the shorter period component coherence images, and it further decreases the quality of the multispectral coherence image using spectral probes (the red circles in Figure 16).

Conclusion

We use a 3D seismic data volume to evaluate four different spectral decomposition methods in multispectral coherence computation. We recommend computing multispectral coherence using exponentially spaced spectral voices because it provides better coherence images than the results using equally spaced components for the same computation cost. The resolution of thinner channels and small-scale features is further improved in multispectral coherence images computed using the maximum entropy spectral voices over the CWT results. The images of the thicker channel boundaries are the most continuous in the coherence computed using the AVT data set, but the quality of small-scale features inside the thicker channels is decreased. Furthermore, multi-

spectral coherence computed using the nonlinear spectral probes appears more balanced to help reveal the small-scale geologic features inside the thicker channel. However, because amplitudes are not preserved in the nonlinear spectral probe decomposition, we use an equal weight for the noise in noisier shorter period components to build the covariance matrix, resulting in increased noise in the multispectral coherence images. Based on the observations in these experiments, we recommend computing multispectral coherence on the spectral voices decomposed using the maximum entropy method. The window length in spectral decomposition plays an important role in the generated coherence images. If we use a longer window, the geology features such as the incised channels are more averaged with greater geologic "overprinting." The influence of window length in different spectral decomposition methods on the channel morphology remains an interesting research topic.

Acknowledgments

Data and materials availability

Data associated with this research are available and can be obtained by contacting the corresponding author.

Appendix A

Coherence computation based on the energy-ratio method

Each element of the covariance matrix is calculated using the analytic trace to avoid the artifacts due to the small windows over the zero crossings:

$$C_{mn} = \sum_{k=-K}^{K} [d(t_k, x_m, y_m)d(t_k, x_n, y_n) + d^H(t_k, x_m, y_m)d^H(t_k, x_n, y_n)], \quad \text{(A-1)}$$

where d denotes the original seismic data, d^H is the corresponding Hilbert transform, C_{mn} represents the element of the covariance matrix, and t_k denotes

the structurally interpolated time sample at a distance (x_m, y_m) from the coordinate origin point.

We then generate the energy-ratio coherence by computing the ratio of the coherent energy E_c and the total energy E_t within an analysis window:

$$s = \frac{E_c}{E_t + \varepsilon^2}, \qquad \text{(A-2)}$$

where ε is a small positive value to avoid division by zero. We define the Karhunen-Loève (KL)-filtered coherent energy and the total energy as

$$E_c = \sum_{m=1}^{M} \sum_{k=-K}^{K} \{[d_{\mathrm{KL}}(t_k, x_m, y_m)]^2 + [d_{\mathrm{KL}}^H(t_k, x_m, y_m)]^2\}, \qquad \text{(A-3)}$$

$$E_t = \sum_{m=1}^{M} \sum_{k=-K}^{K} \{[d(t_k, x_m, y_m)]^2 + [d^H(t_k, x_m, y_m)]^2\}. \quad \text{(A-4)}$$

Appendix B
CWT theory

Grossmann and Morlet (1984) formally introduce that a function with zero mean is called a "wavelet," which has finite energy concentrated in time and satisfies certain well-established conditions. We can generate a family of wavelet functions from a mother wavelet $\psi(t)$, which is centered about $t = 0$, scaled using a dilation factor s, and shifted by time τ:

$$\psi_{s,\tau}(t) = \frac{1}{\sqrt{s}} \psi\left(\frac{t - \tau}{s}\right). \qquad \text{(B-1)}$$

CWT is performed by crosscorrelating the library of wavelets of equation B-1 with a seismic time series:

$$W(\tau, s) = \int_{-\infty}^{+\infty} d(t) \frac{1}{\sqrt{s}} \psi^*\left(\frac{t - \tau}{s}\right) dt, \qquad \text{(B-2)}$$

where $W(\tau, s)$ is the time-scale map, $d(t)$ represents the seismic time series, and $\psi^*((t - \tau)/s)$ is the complex conjugate of $\psi((t - \tau)/s)$. The local spectrum is defined by the crosscorrelation coefficients at each time sample.

Appendix C
Optimized AVT workflow

The optimized AVT workflow is implemented using the following three steps:

1) Envelope calculation from the analytic transform of the seismic data,

$$D(t_i) = d(t_i) + id^{\mathrm{H}}(t_i), \qquad \text{(C-1)}$$

where D is the analytic signal, which is composed by the seismic amplitude d and its Hilbert transform d^{H}.

The envelope is then calculated by taking the magnitude of this analytic signal,

$$E(t_i) = |D(t_i)| = \sqrt{[d(t_i)]^2 + [d^{\mathrm{H}}(t_i)]^2}. \qquad \text{(C-2)}$$

2) Calculation of the rms envelope within a defined window,

$$\bar{E}_{\mathrm{rms}}(t_i) = \sqrt{\frac{\sum_{t_j=t_i-N/2}^{t_j=t_i+N/2} E^2(t_j)}{N}}. \qquad \text{(C-3)}$$

3) Inverse Hilbert transform of the rms envelope,

$$\bar{E}_{\mathrm{AVT}}(t_i) = \mathrm{H}^{-1}\{\bar{E}_{\mathrm{rms}}(t_i)\}. \qquad \text{(C-4)}$$

Appendix D
Spectral probe theory

In the spectral probe technique, we generate the normalized crosscorrelation coefficients between a wavelet $w(t)$ and the seismic amplitude $d(t)$:

$$\rho(t) = \frac{\sum_{j=-J}^{+J} w(t - j\Delta t)d(t - j\Delta t)}{\sqrt{\sum_{j=-J}^{+J}[w(t - j\Delta t)]^2 \sum_{j=-J}^{+J}[d(t - j\Delta t)]^2}}. \qquad \text{(D-1)}$$

We set the wavelet probe using a cosine wave,

$$w(j\Delta t) = \cos(2\pi f j\Delta t), \qquad \text{(D-2)}$$

where f is the frequency, Δt is the sample increment, and j is the sample index. If we choose the correlation range $2J\Delta t = 1/f$, which means exactly one period, equation D-1 could be simplified to

$$\rho(t) = \frac{\sum_{j=-J}^{+J} \cos[2\pi(t - j\Delta t)]d(t - j\Delta t)}{\sqrt{\sum_{j=-J}^{+J}[d(t - j\Delta t)]^2}}. \qquad \text{(D-3)}$$

We produce different data volumes of crosscorrelation coefficients with different periods (or corresponding frequencies) using equation D-3.

References

Alaei, B., 2012, Improved fault imaging by integration of frequency decomposition and fault attributes, example from mid Norwegian sea: Proceedings of the 3rd EAGE Fault and Top Seal Conference, C13, doi: 10.3997/2214-4609.20143024.

Bahorich, M. S., and S. L. Farmer, 1995, 3-D seismic coherency for faults and stratigraphic features: The coherence cube: The Leading Edge, **14**, 1053–1058, doi: 10.1190/1.1437077.

Bulhões, E. M., 1999, Técnica "VOLUME DE AMPLITUDES" para mapeamento de feições estruturais (in

Portuguese): 6th International Congress of the Brazilian Society of Geophysics.

Bulhões, E. M., and W. de Amorin, 2005, Princípio da Sismocamada Elementar e sua Aplicação à Técnica de Volume de Amplitudes (tec. VA) (in Portuguese): 9th International Congress of the Brazilian Geophysical Society.

Bussell, M. R., 1994, Seismic interpretation of the Moki Formation on the Maui 3D survey, Taranaki Basin: Proceedings of the New Zealand Petroleum Conference, Ministry of Economic Development, 240–255.

Castagna, J., S. Sun, and R. Siegfried, 2003, Instantaneous spectral analysis: Detection of low-frequency shadows associated with hydrocarbons: The Leading Edge, **22**, 120–127, doi: 10.1190/INT-2016-0152.1.

Castagna, J. P., and S. Sun, 2006, Comparison of spectral decomposition methods: First Break, **24**, 75–79.

Chopra, S., and K. J. Marfurt, 2007, Seismic attributes for prospect identification and reservoir characterization: SEG.

Chopra, S., and K. J. Marfurt, 2019, Multispectral, multiazimuth, and multioffset coherence attribute applications: Interpretation, **7**, no. 2, SC21–SC32, doi: 10.1190/INT-2018-0090.1.

Davogustto, O., M. C. Matos, C. Cabarcas, T. Dao, and K. J. Marfurt, 2013, Resolving subtle stratigraphic features using spectral ridges and phase residues: Interpretation, **1**, no. 1, SA93–SA108, doi: 10.1190/INT-2013-0015.1.

Dewett, D. T., and A. A. Henza, 2015, Spectral similarity fault enhancement: Interpretation, **4**, no. 1, SB149–SB159, doi: 10.1190/INT-2015-0114.1.

Gao, D., 2013, Wavelet spectral probe for seismic structure interpretation and fracture characterization: A workflow with case studies: Geophysics, **78**, no. 5, O57–O67, doi: 10.1190/geo2012-0427.1.

Gersztenkorn, A., and K. J. Marfurt, 1999, Eigenstructure-based coherence computations as an aid to 3-D structural and stratigraphic mapping: Geophysics, **64**, 1468–1479, doi: 10.1190/1.1444651.

Grossmann, A., and J. Morlet, 1984, Decomposition of Hardy functions into square integrable wavelets of constant shape: SIAM Journal on Mathematical Analysis, **15**, 723–736, doi: 10.1137/0515056.

Hardage, B., 2009, Frequencies are fault finding factors: Looking low aids data interpretation: AAPG Explorer, **30**, 34.

Infante-Paez, L., and K. Marfurt, 2017, Seismic expression and geomorphology of igneous bodies: A Taranaki Basin, New Zealand, case study: Interpretation, **5**, no. 3, SK121–SK140, doi: 10.1190/INT-2016-0244.1.

King, P. R., G. H. Scott, and P. H. Robinson, 1993, Description, correlation and depositional history of Miocene sediments outcropping along North Taranaki coast: Institute of Geological & Nuclear Sciences Ltd., 199.

Laughlin, K., P. Garossino, and G. Partyka, 2002, Spectral decomposition applied to 3D: AAPG Explorer, **23**, 28–31.

Li, F., and W. Lu, 2014, Coherence attribute at different spectral scales: Interpretation, **2**, no. 1, SA99–SA106, doi: 10.1190/INT-2013-0089.1.

Li, F., J. Qi, B. Lyu, and K. J. Marfurt, 2018, Multispectral coherence: Interpretation, **6**, no. 1, T61–T69, doi: 10.1190/INT-2017-0112.1.

Libak, A., B. Alaei, and A. Torabi, 2017, Fault visualization and identification in fault seismic attribute volumes: Implications for fault geometric characterization: Interpretation, **5**, no. 2, B1–B16, doi: 10.1190/INT-2016-0152.1.

Liu, J., and K. J. Marfurt, 2007, Instantaneous spectral attributes to detect channels: Geophysics, **72**, no. 2, P23–P31, doi: 10.1190/1.2428268.

Lubo-Robles, D., and K. J. Marfurt, 2019, Independent component analysis for reservoir geomorphology and unsupervised seismic facies classification in the Taranaki Basin, New Zealand: Interpretation, **7**, no. 3, SE19–SE42, doi: 10.1190/INT-2018-0109.1.

Lyu, B., F. Li, J. Qi, T. Zhao, and K. J. Marfurt, 2018, Highlighting discontinuities with variational mode decomposition based coherence: 88th Annual International Meeting, SEG, Expanded Abstracts, 1798–1802, doi: 10.1190/segam2018-2997710.1.

Lyu, B., J. Qi, G. Machado, F. Li, and K. J. Marfurt, 2019, Seismic fault enhancement using spectral decomposition assisted attributes: 89th Annual International Meeting, SEG, Expanded Abstracts, 1938–1942, doi: 10.1190/segam2019-3215703.1.

Marfurt, K. J., 2017, Interpretational aspects of multispectral coherence: 79th Annual International Conference and Exhibition, EAGE, Extended Abstracts, ThA411, doi: 10.3997/2214-4609.201700528.

Marfurt, K. J., and T. M. Alves, 2014, Pitfalls and limitations in seismic attribute interpretation of tectonic features: Interpretation, **3**, no. 1, SB5–SB15, doi: 10.1190/INT-2014-0122.1.

Marfurt, K. J., S. L. Farmer, M. S. Bahorich, and R. L. Kirlin, 1998, 3-D seismic attributes using a semblance-based coherency algorithm: Geophysics, **63**, 1150–1165, doi: 10.1190/1.1444415.

Marfurt, K. J., and R. Kirlin, 2001, Narrow-band spectral analysis and thin-bed tuning: Geophysics, **66**, 1274–1283, doi: 10.1190/1.1487075.

Marfurt, K. J., V. Sudhaker, A. Gersztenkorn, and K. D. Crawford, 1999, Coherency calculations in the presence of structural dip: Geophysics, **64**, 104–111, doi: 10.1190/1.1444508.

Matos, M. C., and K. J. Marfurt, 2011, Inverse continuous wavelet transform "deconvolution": 81st Annual International Meeting, SEG, Expanded Abstracts, 1861–1865, doi: 10.1190/1.3627569.

Partyka, G. A., J. Gridley, and J. Lopez, 1999, Interpretational applications of spectral decomposition in reservoir characterization: The Leading Edge, **18**, 353–360, doi: 10.1190/1.1438295.

Peyton, L., R. Bottjer, and G. Partyka, 1998, Interpretation of incised valleys using new-3D seismic techniques: A case history using spectral decomposition and coherency: The Leading Edge, 17, 1294–1298, doi: 10.1190/1.1438127.

Pilaar, W. F. H., and L. L. Wakefield, 1984, Hydrocarbon generation in the Taranaki Basin, New Zealand, *in* G. Demaison and R. J. Murris, eds., Petroleum geochemistry and basin evaluation, AAPG Memoir, 35, 405–423.

Portniaguine, O., and J. P. Castagna, 2004, Inverse spectral decomposition: 74th Annual International Meeting, SEG, Expanded Abstracts, 1786–1789, doi: 10.1190/1.1845172.

Puryear, C. I., O. N. Portniaguine, C. M. Cobos, and J. P. Castagna, 2012, Constrained least-squares spectral analysis: Application to seismic data: Geophysics, 77, no. 5, V143–V167, doi: 10.1190/geo2011-0210.1.

Qi, J., F. Li, B. Lyu, B. Zhang, O. Olorunsola, and K. J. Marfurt, 2016, Seismic fault enhancement and skeletonization: 86th Annual International Meeting, SEG, Expanded Abstracts, 1966–1970, doi: 10.1190/segam2016-13876567.1.

Qi, J., B. Lyu, A. Alali, G. Machado, Y. Hu, and K. J. Marfurt, 2019, Image processing of seismic attributes for automatic fault extraction: Geophysics, 84, no. 1, O25–O37, doi: 10.1190/segam2018-2997854.1.

Sinha, S., R. Routh, P. Anno, and J. Castagna, 2005, Spectral decomposition of seismic data with continuous-wavelet transform: Geophysics, 70, no. 6, P19–P25, doi: 10.1190/1.2127113.

Sui, J., X. Zheng, and Y. Li, 2015, A seismic coherency method using spectral attributes: Applied Geophysics, 12, 353–361, doi: 10.1007/s11770-015-0501-5.

Ten Kroode, A. P. E., S. Bergler, C. Corsten, J. W. de Maag, F. Strijbos, and H. Tijhof, 2013, Broadband seismic data — The importance of low frequencies: Geophysics, 78, no. 2, WA3–WA14, doi: 10.1190/geo2012-0294.1.

Vernengo, L., and E. Trinchero, 2015, Application of amplitude volume technique attributes, their variations, and impact: The Leading Edge, 34, 1246–1253, doi: 10.1190/tle34101246.1.

Vernengo, L., E. Trinchero, M. G. Torrejón, and I. Rovira, 2017, Amplitude volume technique attributes and multidimensional seismic interpretation: The Leading Edge, 36, 776–781, doi: 10.1190/tle36090776.1.

Wang, S., S. Yuan, T. Wang, J. Gao, and S. Li, 2018, Three-dimensional geosteering coherence attributes for deep-formation discontinuity detection: Geophysics, 83, no. 6, O105–O113, doi: 10.1190/geo2017-0642.1.

Wang, T., S. Yuan, J. Gao, S. Li, and S. Wang, 2019, Multispectral phase-based geosteering coherence attributes for deep stratigraphic feature characterization: IEEE Geoscience and Remote Sensing Letters, 16, 1309–1313, doi: 10.1109/LGRS.8859.

Yagci, G., 2016, 3D seismic structural and stratigraphic interpretation of the Tui-3D field, Taranaki Basin, New Zealand: Master's thesis, Missouri University of Science and Technology.

Zeng, H., 2015, Predicting geometry and stacking pattern of thin beds by interpreting geomorphology and waveforms using sequential stratal-slices in the Wheeler domain: Interpretation, 3, no. 3, SS49–SS64, doi: 10.1190/INT-2014-0181.1.

Bin Lyu received a B.S. (2003) and an M.S. (2006) in geophysics from China University of Petroleum. He is currently a Ph.D. candidate in geophysics at the University of Oklahoma as a graduate research assistant at the AASPI Consortium. From 2006 to 2015, he served as a processing geophysicist in the Petrochina Research Institute of Petroleum Exploration & Development-Northwest. His current research interests include new seismic attribute development and interpretation, seismic processing, reverse time migration, full-waveform inversion, passive seismic imaging, seismic anisotropy, and seismic attenuation.
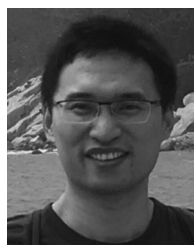
Jie Qi received a B.D. (2011) from China University of Petroleum, Beijing, China, an M.D. (2013) from the University of Houston, and a Ph.D. (2017) in applied geophysics from the University of Oklahoma. From 2011 to 2017, he worked as graduate research assistant at the University of Houston and the University of Oklahoma. He is currently a postdoc research associate at the University of Oklahoma. He is a member of SEG, AAPG, and the Geophysical Societies of Houston. His research interests include machine-learning application, pattern recognition, image processing, seismic attribute development and interpretation, and seismic facies analysis.

Fangyu Li received a Ph.D. (2017) in geophysics from the University of Oklahoma. He is a postdoctoral research associate in the College of Engineering, University of Georgia. His research interests include advanced signal processing, seismic imaging, quantitative interpretation, reservoir characterization, machine learning, deep learning, distributed computing, and cyberphysical systems.
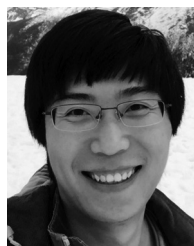
Tao Zhao received a Ph.D. (2017) in geophysics from the University of Oklahoma, where he worked on developing and calibrating pattern recognition and machine-learning techniques applied to multiattribute seismic facies analysis as a graduate research assistant in the AASPI consortium. He is currently a data scientist at Schlumberger. Before his current role at Schlumberger, he was a research geophysicist at Geophysical Insights from 2017

to 2019. His current research interests include developing and applying shallow and deep machine-learning techniques for solving problems in seismic processing, imaging, and interpretation.

Kurt J. Marfurt received a Ph.D. (1978) in applied geophysics from Columbia University's Henry Krumb School of Mines in New York, where he also taught as an assistant professor for four years. He joined the University of Oklahoma (OU) in 2007, where he serves as the Frank and Henrietta Schultz professor of geophysics within the ConocoPhillips School of Geology and Geophysics. He worked for 18 years in a wide range of research projects at Amoco's Tulsa Research Center, after which he joined the University of Houston for eight years as a professor of geophysics and the director of the Allied Geophysics Lab. He has received the following recognitions: SEG best paper (for coherence), SEG best presentation (for seismic modeling), as a coauthor with Satinder Chopra for best SEG poster (for curvature) and best AAPG technical presentation, and as a coauthor with Roderick Perez-Altamar for best paper in *Interpretation* (on a resource play case study). He also served as the SEG/EAGE Distinguished Short Course Instructor for 2006 (on seismic attributes). In addition to teaching and research duties at OU, he leads short courses on attributes for SEG and AAPG. His primary research interests include the development and calibration of new seismic attributes to aid in seismic processing, seismic interpretation, and reservoir characterization. Recent work has focused on applying coherence, spectral decomposition, structure-oriented filtering, and volumetric curvature to mapping fractures and karst with a particular focus on resource plays.

Biographies and photographs of the other authors are not available.